

# Current Biology

## Mechanical Stress and Network Structure Drive Protein Dynamics during Cytokinesis

### Highlights

- Equatorially enriched proteins have reduced mobility at the cleavage furrow
- Mechanical stress felt by the cytoskeleton inhibits equatorial protein dynamics
- Structural changes in cytoskeletal network are sufficient to alter protein dynamics
- Cortical protein dynamics are robust to genetic and mechanical perturbations

### Authors

Vasudha Srivastava, Douglas N. Robinson

### Correspondence

[dnr@jhmi.edu](mailto:dnr@jhmi.edu)

### In Brief

Srivastava and Robinson examine how protein dynamics can explain spatiotemporal changes in protein localization during cytokinesis. The reduced cleavage furrow mobility of many mechanoresponsive, equatorially enriched proteins is dependent on mechanical stress and cytoskeletal structure and is robust to genetic and mechanical perturbations.

## Report

# Mechanical Stress and Network Structure Drive Protein Dynamics during Cytokinesis

Vasudha Srivastava<sup>1,3</sup> and Douglas N. Robinson<sup>1,2,3,\*</sup>

<sup>1</sup>Department of Cell Biology

<sup>2</sup>Department of Pharmacology and Molecular Sciences  
Johns Hopkins University School of Medicine, Baltimore,  
MD 21205, USA

<sup>3</sup>Department of Chemical and Biomolecular Engineering,  
Johns Hopkins University, Baltimore, MD 21218, USA

### Summary

Cell-shape changes associated with processes like cytokinesis and motility proceed on several-second timescales but are derived from molecular events, including protein-protein interactions, filament assembly, and force generation by molecular motors, all of which occur much faster [1–4]. Therefore, defining the dynamics of such molecular machinery is critical for understanding cell-shape regulation. In addition to signaling pathways, mechanical stresses also direct cytoskeletal protein accumulation [5–7]. A myosin-II-based mechanosensory system controls cellular contractility and shape during cytokinesis and under applied stress [6, 8]. In *Dictyostelium*, this system tunes myosin II accumulation by feedback through the actin network, particularly through the crosslinker cortexillin I. Cortexillin-binding IQGAPs are major regulators of this system. Here, we defined the short timescale dynamics of key cytoskeletal proteins during cytokinesis and under mechanical stress, using fluorescence recovery after photobleaching and fluorescence correlation spectroscopy, to examine the dynamic interplay between these proteins. Equatorially enriched proteins including cortexillin I, IQGAP2, and myosin II recovered much more slowly than actin and polar crosslinkers. The mobility of equatorial proteins was greatly reduced at the furrow compared to the interphase cortex, suggesting their stabilization during cytokinesis. This mobility shift did not arise from a single biochemical event, but rather from a global inhibition of protein dynamics by mechanical-stress-associated changes in the cytoskeletal structure. Mechanical tuning of contractile protein dynamics provides robustness to the cytoskeletal framework responsible for regulating cell shape and contributes to cytokinesis fidelity.

### Results and Discussion

#### Equatorial Proteins Have Slower Recovery Times Than Polar Crosslinkers and Exhibit Reduced Mobility at the Cleavage Furrow

The short timescale dynamics of proteins regulate their recruitment and localization. Actin-associated proteins may be classified into two groups: the equatorially enriched cleavage furrow proteins and the polar or globally distributed proteins ([9], Figure 1A). We used fluorescence recovery after photobleaching (FRAP) to examine the dynamics of these groups in interphase and dividing *Dictyostelium* cells, to explain

differences in their spatiotemporal localization. We measured the fluorescence intensity in the bleached region until the recovery curve saturated (10–25 s), allowing accurate calculation of recovery times and immobile fractions for key cytoskeletal proteins (see Supplemental Experimental Procedures; Figures S1A–S1C). The characteristic recovery time is dominated by binding-unbinding rates, while the immobile fraction represents the population that does not turn over during the experiment (Figure 1B). As *Dictyostelium* cells are highly motile, longer acquisitions can show additional long-scale recovery due to cellular motility instead of protein dynamics. Thus, for this study we only measure the fast dynamic recovery and mobility. GFP-actin recovers within a second, establishing the dynamicity of the actin network (Figures 1C and S1D). The cortical actin recovery times and immobile fractions were significantly higher than for GFP or cytoplasmic GFP-actin (Figures 1C and S1D). Thus, cortical GFP-actin dynamics reported by FRAP are dominated by actin filaments, even though ~70% of the total actin (250  $\mu$ M) in *Dictyostelium* cells is monomeric [11].

Polar crosslinkers, including dynacortin and fimbrin, modulate cell mechanics and cortical tension, while equatorial proteins—myosin II and cortexillin I—regulate contractility during cytokinesis [9, 12]. As cytokinesis is largely a mechanical shape change process, several equatorial proteins also mediate cellular responses to externally applied mechanical stresses. The mechanoenzyme, myosin II, is the major driver of contractility and accumulates in response to internally or externally generated mechanical stresses [5–7]. This stress-dependent myosin II accumulation results from cooperative interactions between the actin-bound myosin heads and the actin-bundling protein cortexillin I [4]. Scaffolding proteins IQGAP1 and IQGAP2 bind to cortexillin I [13–15] and regulate myosin II accumulation [6]. IQGAP1 inhibits myosin II recruitment, while IQGAP2 relieves this inhibition. Consequently, the *iqgap1/2* double-null mutant (*iqg1/2*) exhibits enhanced myosin II accumulation under stress. IQGAP2 also transmits mechanical signals to spindle signaling proteins (Kif12/INCENP), promoting symmetric cell division.

Genetic, biochemical, and mechanical studies demonstrated crosstalk between the polar and equatorial modules [10, 16]. However, how these proteins interact dynamically to control these processes is unknown. The molecular events governing cytokinesis, including motor activity, actin filament turnover and rearrangement, and crosslinker interactions, occur at much faster timescales than the associated cell-shape changes. Hence, these short timescale cytoskeletal dynamics must be defined to develop a mechanistic understanding of how cells respond to physical forces.

Interestingly, we observed that actin dynamics changed during cytokinesis as the recovery time increased and the immobile fraction decreased in the furrow (Figures 1D and S1E). In comparison, the dynacortin and fimbrin recovery times at the furrow increased significantly, while their mobility was unaffected (Figure 1D [9]). The polar cortex dynamics of dynacortin and fimbrin were similar to interphase values, while actin showed increased mobility at the poles (data not shown). Myosin II, cortexillin I, and IQGAP2, which localize to the cleavage furrow, recovered more slowly (1.5–5 s) than actin or polar

\*Correspondence: [dnr@jhmi.edu](mailto:dnr@jhmi.edu)

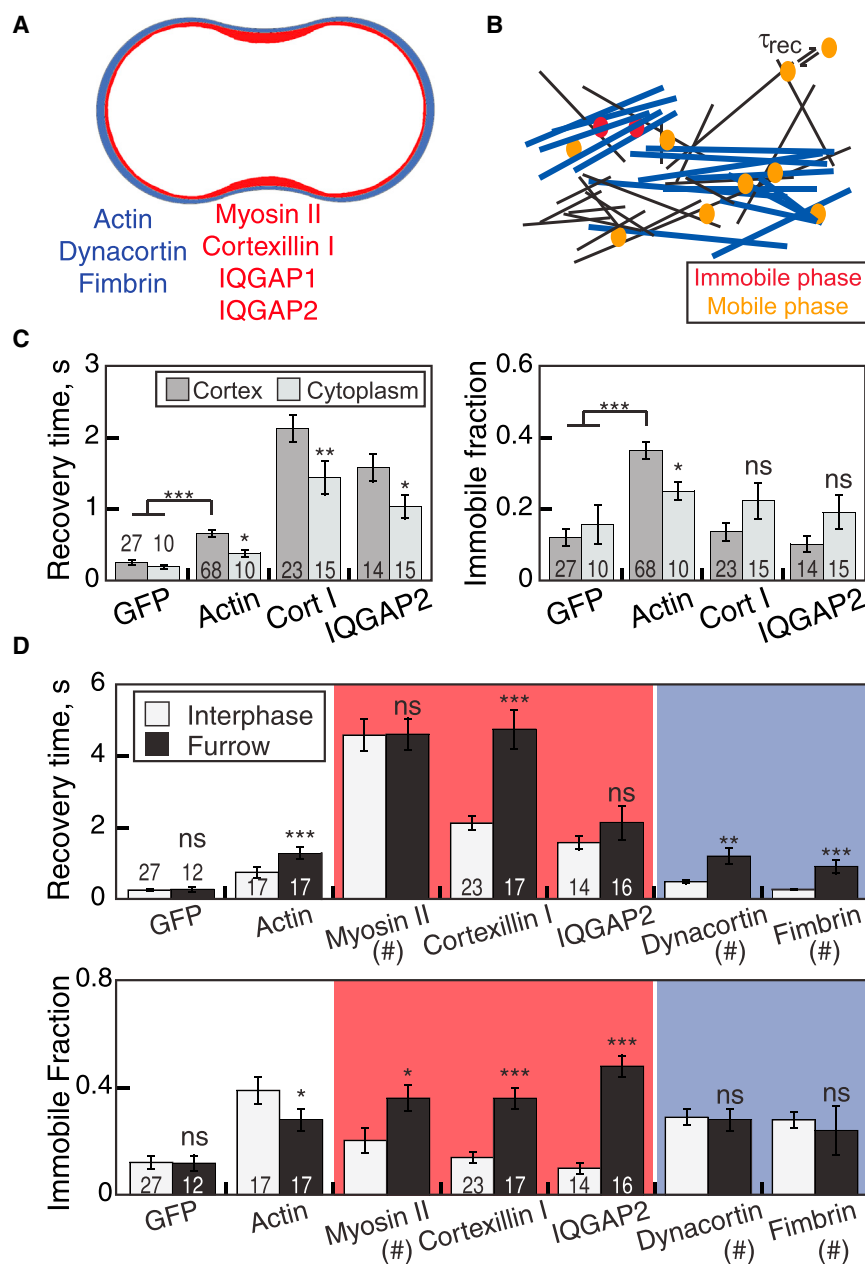


**Figure 1. Changes in Protein Dynamics during Cytokinesis**

(A) Cytoskeletal proteins are asymmetrically localized during cytokinesis.

(B) From FRAP analysis, the network release rate is inversely proportional to the recovery time ( $\tau$ ), while the immobile fraction (dark red circles) represents the protein population that does not turnover during the experiment. The protein mobile fraction is represented by light orange circles. The thick and thin lines represent the immobile and mobile populations of actin, respectively.

(C) Recovery times and immobile fractions for soluble GFP and cytoskeletal proteins at the cell cortex and in the cytoplasm as measured by FRAP. Cytoskeletal proteins show slower recovery in the cortex than in the cytoplasm.

(D) Recovery times and immobile fractions of different cytoskeletal proteins in the interphase cortex and at the cleavage furrow. Equatorially enriched proteins—myosin II, cortexillin I, and IQGAP2—have markedly reduced mobility at the cleavage furrow. Values plotted are mean  $\pm$  SEM; sample sizes are listed on the bars (see Table S1).

Asterisks represent the significance of difference between interphase and furrow measurements where ns,  $p > 0.05$ ; \* $p < 0.05$ ; \*\* $p < 0.005$ ; \*\*\* $p < 0.0005$  based on ANOVA with Fisher's LSD post-test. #FRAP data for myosin II are reproduced from [10] and for dynactin and fimbrin from [9]. See also Figure S1.

increased significantly at the cleavage furrow (Figures 1D and S1C). The magnitude of mobility shift for cortexillin I and IQGAP2 was higher than for myosin II [9, 10, 18]. Thus, we focused on cortexillin I and IQGAP2 dynamics for the remainder of this study. The reduction in protein mobility at the furrow suggests that these proteins are stabilized at the cortex during furrow ingression, consistent with their slower recovery times. The high immobile fractions also likely promote their furrow enrichment. Therefore, determining the factors that cause this mobility shift is essential to

crosslinkers in the interphase cortex (Figures 1D, S2A, and S2B). Their much slower recovery than that of soluble GFP demonstrates that the fluorescence recovery is dominated by unbinding events at the cortex instead of diffusion. Further, their cytoplasmic recovery times are significantly faster than those in the cortex (Figures 1C and S1D), indicating that the equatorial proteins form stable complexes at the cortex with slower unbinding, as compared to polar crosslinkers, which recover more quickly. Cortexillin I recovery was slower at the furrow than in interphase, while myosin II and IQGAP2 showed no change. In contrast, myosin II recovery slows in anaphase as compared to metaphase in *Drosophila* S2 cells [17].

The equatorial proteins were much more mobile during interphase compared to other proteins (Figure 1D). The mobility of cortexillin I and IQGAP2 in the interphase cortex was comparable to those in the cytoplasm (Figures 1C and S1D). However, the immobile fractions for these proteins

explaining how the contractile proteins accumulate and remodel during furrow ingression.

### Genetic Control of Protein Dynamics Is Suppressed at the Furrow

Previous genetic studies established the functional interplay between myosin II, cortexillin I, and the IQGAPs in governing protein accumulation and contractility at the cleavage furrow and in responding to mechanical stress [6] (Figure 2A). Thus, we tested whether the same genetic relationships also dictate protein dynamics, regulating their furrow accumulation. We conducted FRAP on cortexillin I and IQGAP2 at the interphase cortex and the furrow in cell lines lacking key components of this mechanoresponsive system.

Cortexillin I recovery time increased at the furrow compared to the interphase cortex in wild-type (WT) cells (Figures 2B and 2C). However, this slower recovery was not observed in

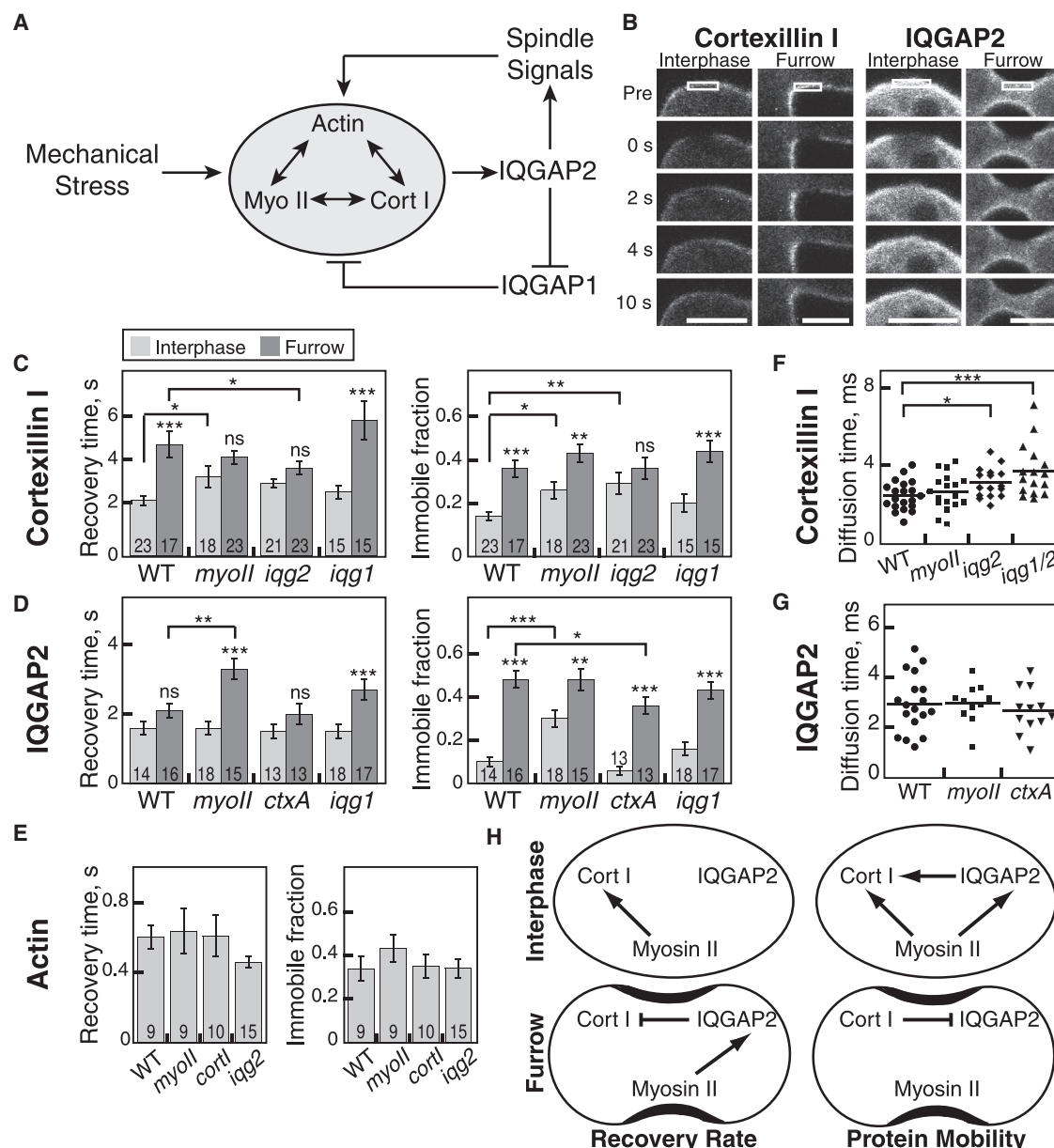


**Figure 2. Changes in Cortexillin I and IQGAP2 Dynamics at the Cleavage Furrow**

(A) A myosin II-cortexillin I-actin-based mechanosensory system regulates contractility at the furrow, and IQGAP proteins regulate accumulation of the contractile proteins.

(B) Confocal images showing photobleaching and fluorescence recovery of GFP-cortexillin I and GFP-IQGAP2 in the cortex of interphase cells and at the cleavage furrow.

(C and D) Recovery times and immobile fractions for GFP-cortexillin I (C) and GFP-IQGAP2 (D) in different genetic mutants in the cortex of interphase and dividing cells.

(E) Recovery times and immobile fractions for GFP-actin in different genetic mutants in the interphase cortex.

(F and G) Cytoplasmic diffusion times measured by FCS for GFP-cortexillin I (F) and GFP-IQGAP2 (G) in different mutants (see Table S3).

(H) Schematic showing the effect of key cytoskeletal proteins on the dynamics of cortexillin I and IQGAP2, based on FRAP measurements. Values plotted are mean  $\pm$  SEM; sample sizes are listed on the bars (see Table S1). p values represented as follows: ns,  $p > 0.05$ ; \* $p < 0.05$ ; \*\* $p < 0.005$ ; \*\*\* $p < 0.0005$  based on ANOVA with Fisher's LSD post-test. Asterisks above the furrow measurement represent significance of difference from interphase values. Comparisons across mutants are represented by asterisks above the connecting lines. Scale bar, 5  $\mu$ m. See also Figure S2.

*myosin II* (*myoII*) and *iqg2* (*iqg2*) -null cells (Figures 2C and S2A). In contrast, while IQGAP2's recovery time was unaltered at the furrow in WT cells, IQGAP2 had significantly higher recovery time at the furrow in *myoII* cells (Figures 2D and S2B). Both cortexillin I and IQGAP2 had >2-fold higher immobile fractions at the cleavage furrow (Figures 2B–2D, S2A, and

S2B). Cortexillin I immobile fractions were higher in interphase *myoII* and *iqg2* compared to WT but were unchanged at the furrow in these mutants (Figures 2C and S2A). This demonstrates that while myosin II and IQGAP2 are important for maintaining a mobile pool of cortexillin I, additional factors such as mechanical stress could dominate cortexillin I mobility

at the furrow, ensuring its recruitment during cytokinesis, as cortaxillin I also shows mechanical-stress-dependent accumulation [6, 7]. Consistently, the cleavage furrow localization of cortaxillin I was not affected in any of the mutants tested. IQGAP2 immobile fraction was also higher in interphase *myoII* as compared to WT (Figures 2D and S2B), suggesting that myosin II drives the dynamic remodeling of the cytoskeletal network. Myosin II's full power stroke is required for this mobility regulation, as the 10-fold slower S456L mutant myosin II, which only takes a 2-nm step (1/4 of WT) [7, 9, 19], fails to rescue the IQGAP2 and cortaxillin I mobility defects seen in *myoII* cells (Figures S2C and S2D). Although myosin II regulates the actin cortex dynamics in epithelial cells [20, 21], deletion of myosin II, cortaxillin I, or IQGAP2 had no impact on actin dynamics (Figures 2E and S2E).

The deletion of IQGAP1 (*iqg1*) did not affect the interphase or furrow dynamics of either cortaxillin I or IQGAP2 (Figures 2C and 2D), in agreement with its role as a damper of stress-dependent protein accumulation [6]. Because IQGAP1 and IQGAP2 interact with distinct domains of cortaxillin I [13–15], we also studied cortaxillin I dynamics in the *iqg1/2* double mutant. Here, cortaxillin I still showed faster recovery at the furrow as compared to WT, similar to *iqg2* (Figures S2F and S2G). However, the immobile fraction at the furrow was higher in the double mutant compared to the WT or *iqg2* mutant (Figures S2F and S2G). The *iqg1/2* cells show enhanced stress-dependent protein accumulation, while *iqg2* cells are unresponsive due to IQGAP1 inhibition [6]. Thus, the reduced mobility of cortaxillin I at the furrow is likely due to mechanical stresses locking in the cytoskeletal network of these highly mechanoresponsive cells.

To examine molecular scale events driving the protein dynamics changes, we used fluorescence correlation spectroscopy (FCS) to measure the in vivo diffusion of cortaxillin I and IQGAP2 across various mutant backgrounds (see Supplemental Experimental Procedures; Figures S1F–S1H). FCS experiments were performed in the cytoplasm as cell movement precluded positioning the confocal volume at the cortex. We compared the diffusion time for cortaxillin I and GFP in the cytoplasm to that of purified proteins in vitro. GFP had 5-fold reduction in diffusion time in cells while cortaxillin I showed >8-fold slower diffusion (Figure S1H), confirming that cortaxillin I is a part of large molecular assemblies. The deletion of myosin II did not impact the cytoplasmic diffusion of either cortaxillin I or IQGAP2 though it increased the immobile fraction of both proteins at the cortex (Figures 2F and 2G), implying that myosin II affects protein dynamics by regulating contractility and cytoskeletal structure. The diffusion time for cortaxillin I was increased by ~30% in *iqg2* cells (Figure 2F). This suggests that without IQGAP2, the effective mass of the cortaxillin I complex roughly doubles as diffusion time is approximately proportional to the cube root of the effective molecular weight of the diffusing species. As expected, cortaxillin I diffusion also showed a similar trend in the *iqg1/2* double mutant. Thus, the changes in cortaxillin I mobility could arise from changes in biochemical interactions in the absence of IQGAP2 (Figures 2C and S2F).

Collectively, the FRAP and FCS experiments enabled us to attribute changes in cortaxillin I mobility to either protein-protein interactions (in *iqg2* and *iqg1/2*) or to cortex restructuring (in *myoII*). We demonstrated that the dynamics of cortaxillin I and IQGAP2 at the cleavage furrow are well conserved across mutants, though differences emerge during interphase (Figure 2H). As cleavage furrow contractility is common to all cells, we hypothesized that mechanical stresses acting at the furrow

could override the biochemical signals to define cleavage furrow protein dynamics. Physical mechanisms such as myosin-II-mediated force generation, Laplace pressure-mediated furrow thinning, and protrusive forces from the polar cortex drive furrow ingression [22]. Thus, we next examined whether mechanical stresses at the cleavage furrow were sufficient to shift the dynamics of these mechanoresponsive proteins.

### Mechanical Stress Drives the Reduction in Cleavage Furrow Mobility of Cortaxillin I and IQGAP2

In addition to enrichment at the cleavage furrow, myosin II, cortaxillin I, and IQGAP2 accumulate to sites of externally applied mechanical stress, thereby allowing the cell to retract against this stress [5–7]. Hence, we applied compression using agarose overlay to test if mechanical stress, as compared to biochemical signaling, affects protein dynamics changes at the cleavage furrow. Flattening of the cells drives the accumulation of the mechanoresponsive proteins studied here to the cell cortex to counter this stress [3, 6]. The ratio of fluorescence intensity in the cortex to that in the cytoplasm is dependent on the thickness of agarose and plating density (T. Luo and D.N.R., unpublished data), confirming that the increase in cortical intensity is driven by mechanical stress and is not simply due to volume effects. Further, soluble GFP does not change in cortical intensity upon compression [6].

We examined cortaxillin I and IQGAP2 interphase dynamics in presence or absence of compression across mutants studied above (Figure 3A). Cortaxillin I exhibited a slower recovery time under compression, but IQGAP2's recovery time was unaffected (Figures 3B, 3C, S3A, and S3B). Both cortaxillin I and IQGAP2 showed a >2-fold increase in the immobile fraction under compression, similar to the observation at the furrow (Figures 3B, 3C, S3A, and S3B). By FCS, the cortaxillin I diffusion time also doubled under compression, while IQGAP2 diffusion was unaffected (Figure 3D). Both the recovery time and immobile fraction for IQGAP2 increased in compressed *myoII* compared to WT (Figures 3C and S3B). Cortaxillin I and IQGAP2 dynamics under compression did not change in other mutants as compared to WT (Figures 3B, 3C, 3F, S3A, and S3B). The cortaxillin I mobility shift in *iqg2* cells under compression was higher than that observed at the furrow (Figure 2C), suggesting that under compression cortaxillin I directly responds to mechanical stress, compared to the cleavage furrow where biochemical signals through IQGAP2 also contribute to cortaxillin I mobility. Importantly, both compression and cleavage furrow showed a consistent, >2-fold increase in immobile fractions of both cortaxillin I and IQGAP2 compared to the unstressed, interphase cortex across various mutants (Figures 2C, 2D, 3B, and 3C). This validates the importance of mechanical stress in driving the dynamics of equatorially enriched proteins at the cleavage furrow, thereby ensuring their robust localized accumulation. In addition, by measuring dynamics of cortaxillin I and IQGAP2 in cells lacking the small GTPase *racE* (*racE*), we assessed the contribution of cortical tension on protein dynamics, as *racE* is a major regulator of cortical mechanics [9, 23, 24]. For cortaxillin I, the immobile fraction was higher and the recovery time was shorter in *racE* cells, while IQGAP2 dynamics were unchanged (Figures S3D and S3E). Thus, cortaxillin dynamics are not only affected by mechanical stress, but also by general cortical mechanics. Furthermore, the mobility and recovery times of GFP-actin were not affected by compression (Figure S1E). Overall, cortaxillin I dynamics are more sensitive



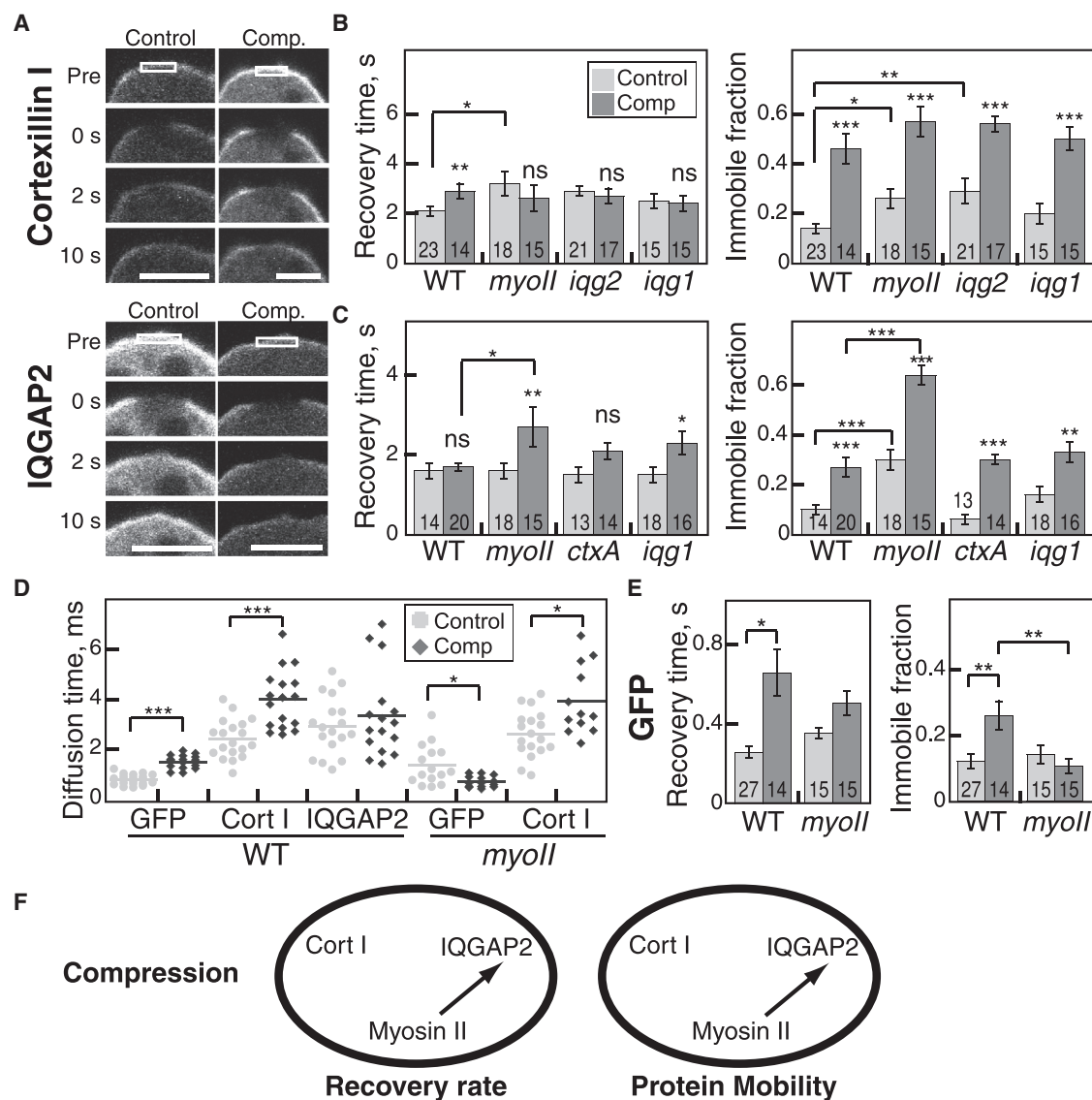


Figure 3. Mechanical Stress Drives Changes in Dynamics and Mobility of Cortesillin I and IQGAP2

(A) Confocal images showing photobleaching and fluorescence recovery of GFP-cortesillin I and GFP-IQGAP2 in the cortex of uncompressed cells (control) and cells compressed using agarose overlay (comp).  
 (B and C) Recovery times and immobile fractions for GFP-cortesillin I (B) and IQGAP2 (C) in different genetic mutants in absence or presence of compressive stress.  
 (D) Cytoplasmic protein diffusion in absence or presence of compressive stress.  
 (E) Recovery times and immobile fractions for GFP in WT and *myoII* cells in absence or presence of compressive stress.  
 (F) Schematic showing the effect of key cytoskeletal proteins on the dynamics of cortesillin I and IQGAP2 under compression, based on FRAP measurements.

Values plotted are mean  $\pm$  SEM; sample sizes are listed on the bars (see Table S1). p values represented as follows: ns,  $p > 0.05$ ; \* $p < 0.05$ ; \*\* $p < 0.005$ ; \*\*\* $p < 0.0005$  based on ANOVA with Fisher's LSD post-test. Asterisks above the compression measurement represent significance of difference from the control. Comparisons across mutants are represented by asterisks above the connecting lines. Scale bar, 5  $\mu$ m. See also Figure S3.

to compressive stresses than the dynamics of IQGAP2, actin, and GFP are.

As compression reduced cell height by up to 4-fold, we measured GFP dynamics to examine the impact of altered protein transport and cellular structure upon compression. The immobile fraction and diffusion time for GFP nearly doubled (Figures 3D, 3E, and S3C), suggesting sieving effects may become significant under compression. The altered GFP dynamics under compression confirm that network structure and intracellular environment are important contributors to

mechanical-stress-dependent protein dynamics. However, in *myoII* cells, GFP FRAP dynamics did not change upon compression; rather, GFP diffusion was faster in compressed *myoII* cells (Figures 3D, 3E, and S3C), suggesting that myosin II is important for stabilizing the cortex under mechanical stress, and in its absence the cortical dynamics are dominated by passive diffusive behaviors [25]. As the actin cytoskeleton forms a highly dense meshwork in *Dictyostelium*, structural changes between interphase and furrow cortex cannot be resolved by confocal and electron microscopy [9]. Thus, we

next chemically perturbed the cytoskeleton to determine how these network properties affect protein mobility and dynamics.

### Alterations to Cortical Structure and Mechanics Shift Mobility of Cortesillin I

To test the effect of cytoskeletal structure on protein dynamics, we perturbed the actin cytoskeleton by treating the cells with either latrunculin-A or jasplakinolide. Latrunculin-A prevents F-actin assembly by sequestering free G-actin monomers, while jasplakinolide enhances actin filament nucleation. We quantified changes in F-actin amount upon treatment with latrunculin-A and jasplakinolide by measuring the relative fluorescence intensity of cells stained with phalloidin 15 min post-drug treatment [4] (Figures 4A, 4B, and S4A). Anti-actin staining was also used to visualize changes in actin level and cytoskeletal morphology (Figures 4A, 4B, and S4A). Interestingly, even with 5  $\mu$ M latrunculin-A, cells still had  $\sim$ 50% residual F-actin ( $\sim$ 35  $\mu$ M) (Figure 4B), suggesting sufficient F-actin binding sites for the  $\sim$ 1  $\mu$ M actin crosslinkers [3, 26, 27]. The residual F-actin mostly concentrated in puncta illustrating discontinuity of the cytoskeletal network (Figure 4A), also reflected by the increase in the recovery time and immobile fraction of GFP even though its diffusion is unaffected (Figures 4D, 4E, and S4D). Latrunculin-A had a drastic effect on cellular mechanics, as 1  $\mu$ M latrunculin-A-treated cells had 12-fold lower cortical tension as measured by micropipette aspiration (Figures 4C, S4B, and S4C), consistent with the 85% reduction in viscoelasticity previously reported for latrunculin-B treatment [12]. Latrunculin-A-treated (5  $\mu$ M) cells were too soft for mechanical measurements. In contrast, jasplakinolide enhanced the cellular F-actin levels  $\sim$ 4-fold inducing the formation of F-actin clusters (Figures 4A, 4B, and S4A) and increased cortical tension slightly (Figures 4C, S4B, and S4C). Jasplakinolide also increased the recovery time of soluble GFP while not affecting its immobile fraction or diffusion (Figures 4D and S4D). Thus, we were able to directly probe the impact of changes in cytoskeletal structure and mechanics on protein dynamics by using these two compounds.

Latrunculin-A or jasplakinolide treatment did not significantly affect cortesillin I recovery time, but both compounds appreciably increased its immobile fraction (Figures 4D and S4D). Latrunculin-A also increased the recovery time and immobile fraction of IQGAP2 (Figures 4D and S4D). IQGAP2 diffusion was insensitive to both drugs (Figure 4E). However, cortesillin I showed two differently diffusing populations with latrunculin-A treatment—one with a similar diffusion time as the control ( $\sim$ 2 ms) and another much slower population ( $\sim$ 8 ms) (Figure 4E). This slower population likely reflects the diffusion of cortesillin I in actin clusters observed upon F-actin staining. Though jasplakinolide treatment promoted F-actin cluster formation, its effect on protein dynamics was not as pronounced (Figures 4D, 4E, and S4D). These results demonstrate that the connectivity of the cytoskeleton network is extremely important for maintaining normal protein dynamics. Remarkably, cortesillin I remained localized at the furrow in latrunculin-A-treated cells, though its distribution was non-uniform (Figure 4F). Its recovery time and mobility in the furrow were unaffected by latrunculin-A (Figures 4G and S4E). Thus, the cortesillin I immobile fraction under mechanical stress is either saturated or becomes independent of network structure. In contrast, myosin II completely lost its cortical localization upon latrunculin-A treatment and formed puncta throughout the cell [4].

Latrunculin-A also increased actin mobility and recovery rate, while jasplakinolide had no effect (Figures 4D and S4D). The increased actin mobility with latrunculin-A is quantitatively similar to that at the furrow (Figures 1D and 4D), further validating the importance of cytoskeletal restructuring during cytokinesis (Figure 4H). These dynamic features also explain why actin does not show a significant accumulation at the cleavage furrow or upon micropipette aspiration [3, 9]. Overall, perturbations to the cytoskeletal structure are sufficient to affect changes in the dynamics of cytoskeletal proteins. Similarly, protein dynamics are also affected by mechanical stress, which leads to accumulation of equatorial proteins during cytokinesis (Figure 4H).

### Conclusions

Mechanical stresses are important for driving cellular processes like cell division and motility and play a major role in determining cell fate [6, 28, 29]. Understanding the effect of mechanical stress on protein dynamics is critical for having predictive power over these cellular behaviors. Here, we identified that equatorial protein mobility significantly reduces at the cleavage furrow, while that of polar crosslinkers is unchanged (Figure 1). Both biochemical associations and myosin II-mediated remodeling affect protein dynamics (Figure 2). Compressive stress applied externally also leads to reduced mobility (Figure 3). The molecular mechanisms that result in this drastic reduction in protein mobility need to be examined. Even when key contractile proteins are eliminated, the cytoskeleton is capable of maintaining fairly normal dynamics (Figures 2 and 3). Interestingly, most of the mutant phenotypes in protein dynamics are seen in the unstressed, interphase cortex, while the dynamics are unchanged across mutants during cytokinesis or upon compression (Figures 2 and 3). Thus, the cell's contractile system is built as a highly adaptive machine, maintaining fairly normal dynamics under mechanical stress ensuring fidelity of protein recruitment. In contrast, in other scenarios mechanical stress can exaggerate many mutant phenotypes. For example, *myoII*-null cells cannot perform cytokinesis without substrate adhesion or when challenged by mechanical stress [5, 30]. Further, changes to cytoskeletal structure are sufficient to drive similar changes in protein dynamics, highlighting the importance of network properties in governing protein and cellular behaviors (Figure 4). Myosin II emerges as the major driver of active processes in the cortex, in accordance with previous studies (Figures 2 and 3) [25].

The mechanical tuning of protein dynamics and recruitment is an important mode of regulating cellular responses to physical stimuli and requires protein-protein interactions to be stabilized or disrupted under mechanical load. Protein-protein stabilization can induce protein clustering and provide signal amplification, while disruption can lead to signal dissipation. This is the classical paradigm for any signal transduction system. Basic molecular mechanisms for protein clustering in response to mechanical stress include catch bond formation and structural cooperativity, while slip bonds allow for force-induced disassembly. These fundamentals are important in directing macromolecular assembly of actin crosslinking proteins [3, 4, 31, 32]. Here we have demonstrated that these mechanisms are also applicable to scaffolding proteins like IQGAP2, emphasizing the importance of network structure and higher order self-assembly in governing cellular behavior. Indeed, cellular systems are engineered as smart materials where many of the constituents are mechanoresponsive.

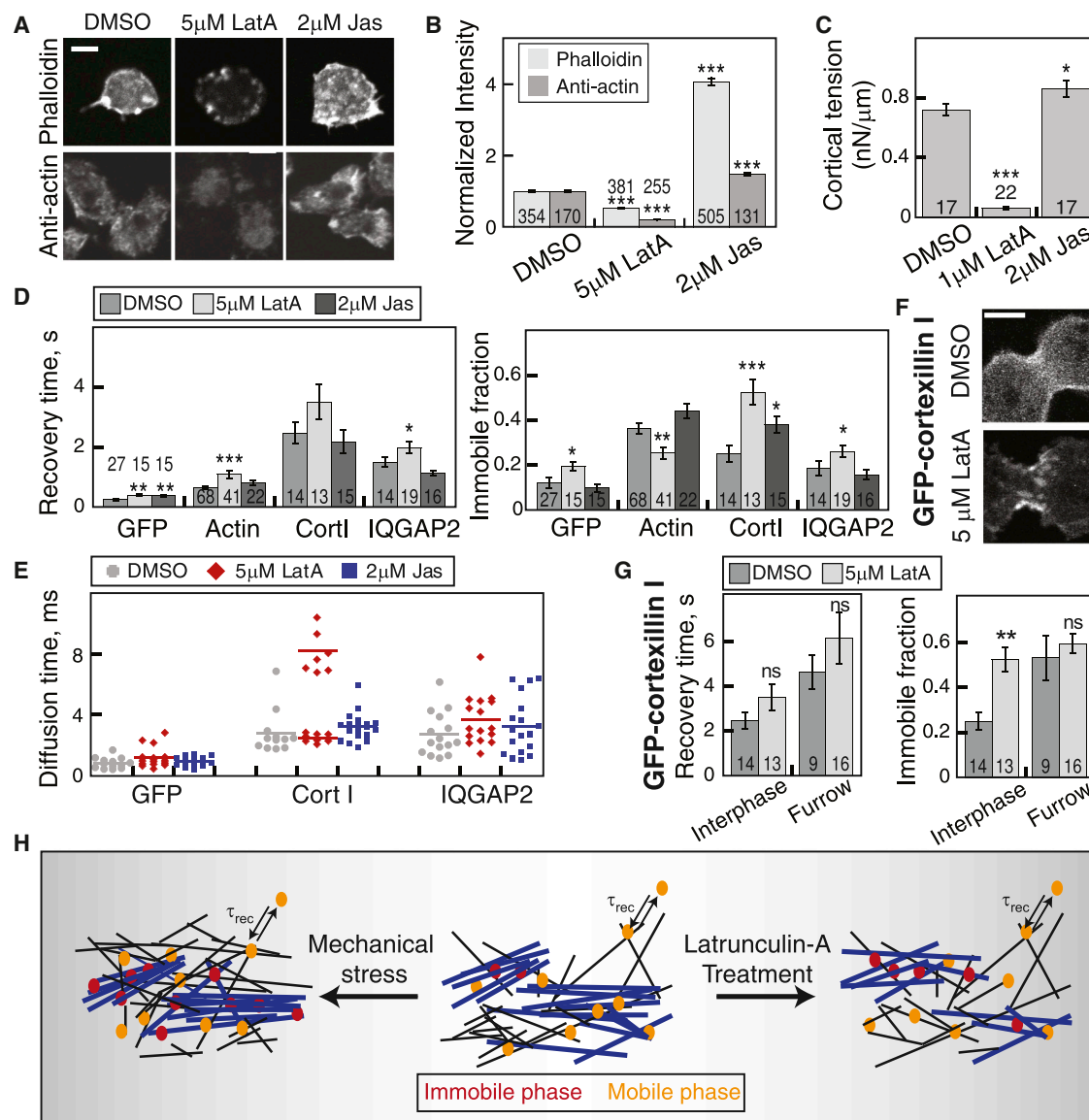


Figure 4. Changes in Cytoskeletal Network Structure Result in Altered Protein Dynamics

(A) Confocal images of TRITC-phalloidin and anti-actin stained cells show changes in the cytoskeletal architecture 15 min post-treatment with 5 μM latrunculin-A or 2 μM jasplakinolide.

(B) Quantification of relative F-actin amount based on the fluorescence intensity of TRITC-phalloidin and anti-actin staining.

(C) Cortical tension measured by micropipette aspiration on cells treated with 1 μM latrunculin-A or 2 μM jasplakinolide.

(D) Recovery times and immobile fractions of soluble GFP, GFP-actin, GFP-cortexillin I, and GFP-IQGAP2 in untreated, 5 μM latrunculin A, or 2 μM jasplakinolide-treated cells as measured by FRAP (see Table S2).

(E) Diffusion times for GFP, GFP-cortexillin I, and GFP-IQGAP2 in untreated, 5 μM latrunculin-A, or 2 μM jasplakinolide-treated cells as measured by FCS (see Table S3). Cortexillin I shows two differently diffusing populations upon latrunculin-A treatment, while the diffusion of GFP and IQGAP2 is unaffected by the pharmacological treatment.

(F) Confocal images showing cleavage furrow recruitment of GFP-cortexillin I in untreated and 5 μM latrunculin-A-treated cells.

(G) Recovery times and immobile fractions of GFP-cortexillin I in interphase and dividing cells with or without 5 μM latrunculin-A treatment.

(H) A schematic showing the changes in protein mobility arise from cytoskeletal rearrangement under mechanical stress or upon latrunculin-A treatment. Under high stress, the crosslinkers show reduced mobility leading to accumulation, while actin mobility increases even though filament amount is relatively unchanged. Upon latrunculin-A treatment, F-actin amount is reduced, and actin mobility increases while the crosslinker mobility decreases significantly. Values plotted are mean ± SEM; sample sizes are listed on the bars (see Table S2). Asterisks represent significance of difference from DMSO control, where p values represented as follows: ns,  $p > 0.05$ ; \* $p < 0.05$ ; \*\* $p < 0.005$ ; \*\*\* $p < 0.0005$  based on ANOVA with Fisher's LSD post-test. Scale bar, 5 μm. See also Figure S4.

## Experimental Procedures

Experimental procedures for *Dictyostelium* cell culture, agarose overlay, FRAP analysis, FCS analysis, latrunculin-A and jasplakinolide treatment, F-actin quantification by phalloidin staining, and cortical

tension measurements by micropipette aspiration are given in Supplemental Experimental Procedures. All curve fitting and statistical analysis was done using KaleidaGraph (Synergy Software). Significance of difference was determined using ANOVA with a Fisher's LSD post-test.



## Supplemental Information

Supplemental Information includes Supplemental Experimental Procedures, four figures, and four tables and can be found with this article online at <http://dx.doi.org/10.1016/j.cub.2015.01.025>.

## Author Contributions

V.S. and D.N.R. designed the experiments, analyzed the data, and prepared the manuscript. V.S. conducted the experiments.

## Acknowledgments

We thank members of D.N.R.'s lab for their valuable comments during manuscript preparation. This work was funded by the Hay Graduate Fellowship Fund (Cell Biology, JHU) (to V.S.), NIH grant GM66817 (to D.N.R.), NIH grant S10 OD016374 (to the JHU Microscope Facility), and the Johns Hopkins Physical Sciences in Oncology Center.

Received: August 19, 2014

Revised: November 12, 2014

Accepted: January 9, 2015

Published: February 19, 2015

## References

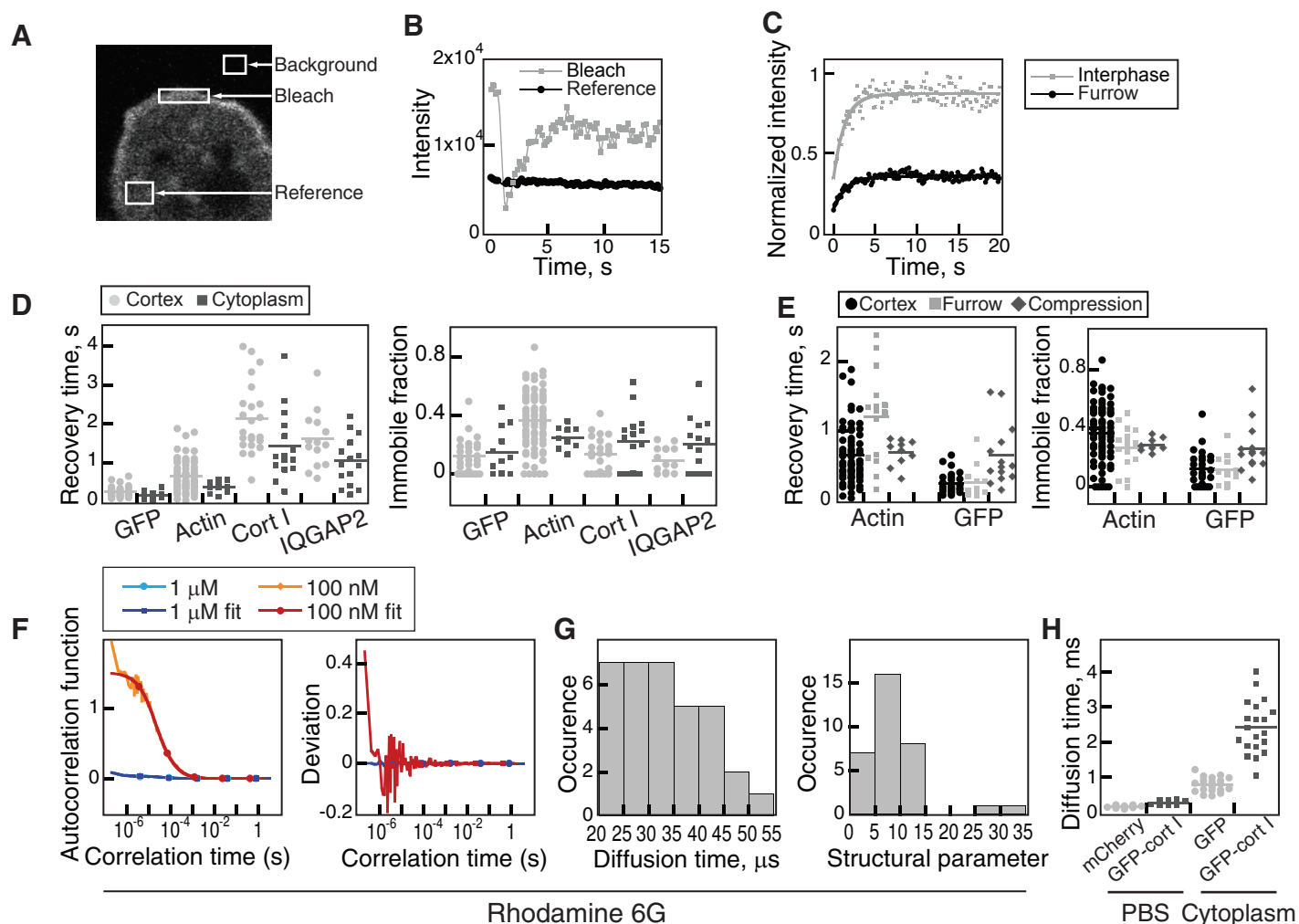
- Craig, E.M., Van Goor, D., Forscher, P., and Mogilner, A. (2012). Membrane tension, myosin force, and actin turnover maintain actin treadmill in the nerve growth cone. *Biophys. J.* **102**, 1503–1513.
- Engl, W., Arasi, B., Yap, L.L., Thiery, J.P., and Viasnoff, V. (2014). Actin dynamics modulate mechanosensitive immobilization of E-cadherin at adherens junctions. *Nat. Cell Biol.* **16**, 587–594.
- Luo, T., Mohan, K., Iglesias, P.A., and Robinson, D.N. (2013). Molecular mechanisms of cellular mechanosensing. *Nat. Mater.* **12**, 1064–1071.
- Luo, T., Mohan, K., Srivastava, V., Ren, Y., Iglesias, P.A., and Robinson, D.N. (2012). Understanding the cooperative interaction between myosin II and actin cross-linkers mediated by actin filaments during mechanosensation. *Biophys. J.* **102**, 238–247.
- Effler, J.C., Kee, Y.-S., Berk, J.M., Tran, M.N., Iglesias, P.A., and Robinson, D.N. (2006). Mitosis-specific mechanosensing and contractile-protein redistribution control cell shape. *Curr. Biol.* **16**, 1962–1967.
- Kee, Y.-S., Ren, Y., Dorfman, D., Iijima, M., Firtel, R., Iglesias, P.A., and Robinson, D.N. (2012). A mechanosensory system governs myosin II accumulation in dividing cells. *Mol. Biol. Cell* **23**, 1510–1523.
- Ren, Y., Effler, J.C., Norstrom, M., Luo, T., Firtel, R.A., Iglesias, P.A., Rock, R.S., and Robinson, D.N. (2009). Mechanosensing through cooperative interactions between myosin II and the actin crosslinker cortexillin I. *Curr. Biol.* **19**, 1421–1428.
- Fernandez-Gonzalez, R., Simoes, Sde.M., Röper, J.-C., Eaton, S., and Zallen, J.A. (2009). Myosin II dynamics are regulated by tension in intercalating cells. *Dev. Cell* **17**, 736–743.
- Reichl, E.M., Ren, Y., Morpheus, M.K., Delannoy, M., Effler, J.C., Girard, K.D., Divi, S., Iglesias, P.A., Kuo, S.C., and Robinson, D.N. (2008). Interactions between myosin and actin crosslinkers control cytokinesis contractility dynamics and mechanics. *Curr. Biol.* **18**, 471–480.
- Zhou, Q., Kee, Y.-S., Poirier, C.C., Jelinek, C., Osborne, J., Divi, S., Surcel, A., Will, M.E., Eggert, U.S., Müller-Taubenberger, A., et al. (2010). 14-3-3 coordinates microtubules, Rac, and myosin II to control cell mechanics and cytokinesis. *Curr. Biol.* **20**, 1881–1889.
- Haugwitz, M., Noegel, A.A., Karakesisoglou, J., and Schleicher, M. (1994). Dictyostelium amoebae that lack G-actin-sequestering profilins show defects in F-actin content, cytokinesis, and development. *Cell* **79**, 303–314.
- Girard, K.D., Chaney, C., Delannoy, M., Kuo, S.C., and Robinson, D.N. (2004). Dynactin contributes to cortical viscoelasticity and helps define the shape changes of cytokinesis. *EMBO J.* **23**, 1536–1546.
- Faix, J., Weber, I., Mintert, U., Köhler, J., Lottspeich, F., and Marriott, G. (2001). Recruitment of cortexillin into the cleavage furrow is controlled by Rac1 and IQGAP-related proteins. *EMBO J.* **20**, 3705–3715.
- Lee, S., Shen, Z., Robinson, D.N., Briggs, S., and Firtel, R.A. (2010). Involvement of the cytoskeleton in controlling leading-edge function during chemotaxis. *Mol. Biol. Cell* **21**, 1810–1824.
- Mondal, S., Burgute, B., Rieger, D., Müller, R., Rivero, F., Faix, J., Schleicher, M., and Noegel, A.A. (2010). Regulation of the actin cytoskeleton by an interaction of IQGAP related protein GAPA with filamin and cortexillin I. *PLoS ONE* **5**, e15440.
- Robinson, D.N., Kee, Y.S., Luo, T., and Surcel, A. (2012). 7.5 understanding how dividing cells change shape. In *Comprehensive Biophysics*, E.H. Egelman, ed. (Amsterdam: Elsevier), pp. 48–72.
- Uehara, R., Goshima, G., Mabuchi, I., Vale, R.D., Spudich, J.A., and Griffith, E.R. (2010). Determinants of myosin II cortical localization during cytokinesis. *Curr. Biol.* **20**, 1080–1085.
- Yumura, S. (2001). Myosin II dynamics and cortical flow during contractile ring formation in Dictyostelium cells. *J. Cell Biol.* **154**, 137–146.
- Murphy, C.T., Rock, R.S., and Spudich, J.A. (2001). A myosin II mutation uncouples ATPase activity from motility and shortens step size. *Nat. Cell Biol.* **3**, 311–315.
- Guha, M., Zhou, M., and Wang, Y.L. (2005). Cortical actin turnover during cytokinesis requires myosin II. *Curr. Biol.* **15**, 732–736.
- Murthy, K., and Wadsworth, P. (2005). Myosin-II-dependent localization and dynamics of F-actin during cytokinesis. *Curr. Biol.* **15**, 724–731.
- Poirier, C.C., Ng, W.P., Robinson, D.N., and Iglesias, P.A. (2012). Deconvolution of the cellular force-generating subsystems that govern cytokinesis furrow ingression. *PLoS Comput. Biol.* **8**, e1002467.
- Robinson, D.N., and Spudich, J.A. (2000). Dynactin, a genetic link between equatorial contractility and global shape control discovered by library complementation of a Dictyostelium discoideum cytokinesis mutant. *J. Cell Biol.* **150**, 823–838.
- Zhang, W., and Robinson, D.N. (2005). Balance of actively generated contractile and resistive forces controls cytokinesis dynamics. *Proc. Natl. Acad. Sci. USA* **102**, 7186–7191.
- Girard, K.D., Kuo, S.C., and Robinson, D.N. (2006). Dictyostelium myosin II mechanochemistry promotes active behavior of the cortex on long time scales. *Proc. Natl. Acad. Sci. USA* **103**, 2103–2108.
- Faix, J., Steinmetz, M., Boves, H., Kammerer, R.A., Lottspeich, F., Mintert, U., Murphy, J., Stock, A., Aebi, U., and Gerisch, G. (1996). Cortexillins, major determinants of cell shape and size, are actin-bundling proteins with a parallel coiled-coil tail. *Cell* **86**, 631–642.
- Robinson, D.N., Ocon, S.S., Rock, R.S., and Spudich, J.A. (2002). Dynactin is a novel actin bundling protein that localizes to dynamic actin structures. *J. Biol. Chem.* **277**, 9088–9095.
- Bastounis, E., Meili, R., Álvarez-González, B., Francois, J., del Álamo, J.C., Firtel, R.A., and Lasheras, J.C. (2014). Both contractile axial and lateral traction force dynamics drive amoeboid cell motility. *J. Cell Biol.* **204**, 1045–1061.
- Engler, A.J., Sen, S., Sweeney, H.L., and Discher, D.E. (2006). Matrix elasticity directs stem cell lineage specification. *Cell* **126**, 677–689.
- De Lozanne, A., and Spudich, J.A. (1987). Disruption of the Dictyostelium myosin heavy chain gene by homologous recombination. *Science* **236**, 1086–1091.
- Thomas, W.E., Vogel, V., and Sokurenko, E. (2008). Biophysics of catch bonds. *Annu. Rev. Biophys.* **37**, 399–416.
- Ferrer, J.M., Lee, H., Chen, J., Pelz, B., Nakamura, F., Kamm, R.D., and Lang, M.J. (2008). Measuring molecular rupture forces between single actin filaments and actin-binding proteins. *Proc. Natl. Acad. Sci. USA* **105**, 9221–9226.

Current Biology

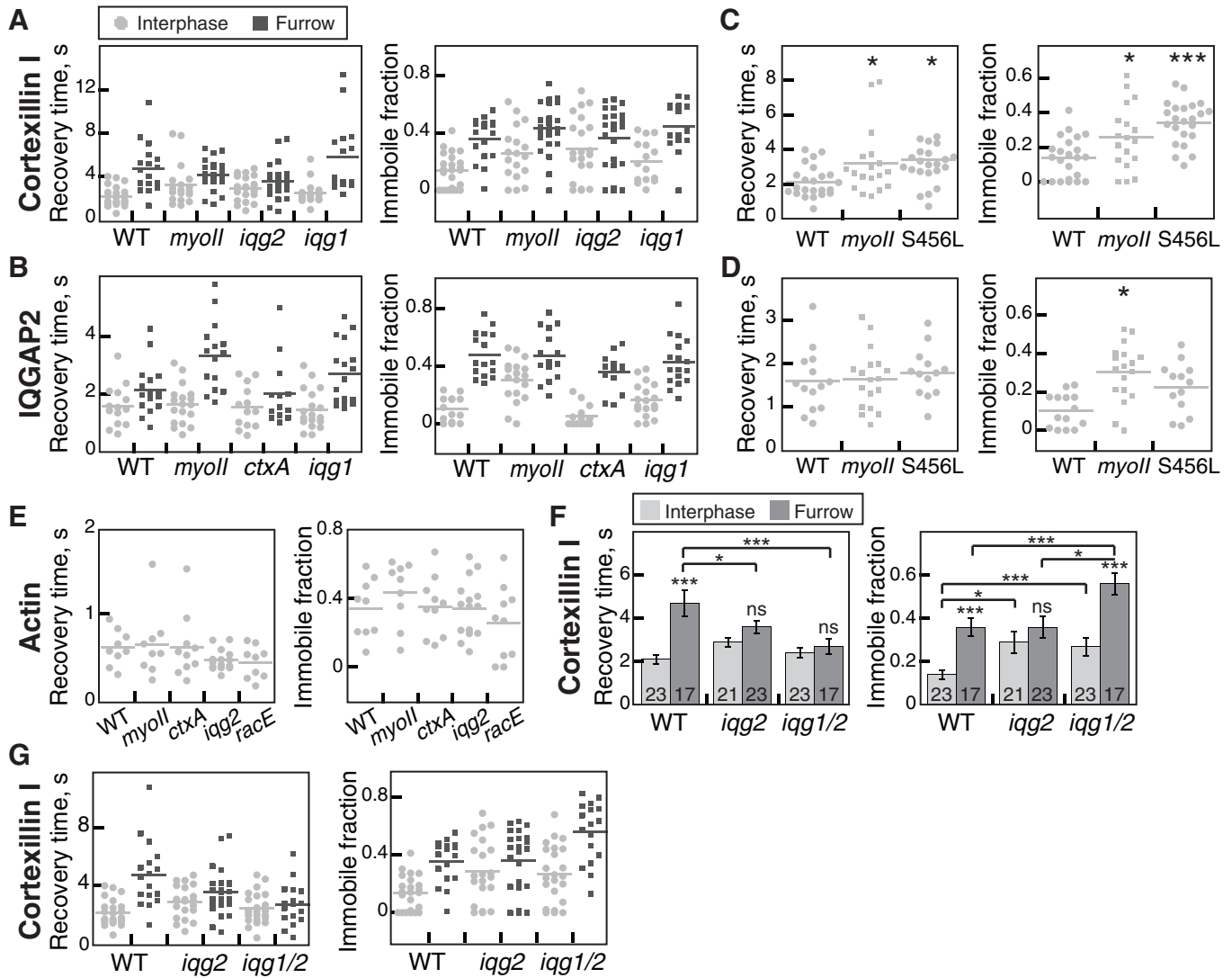
Supplemental Information

# **Mechanical Stress and Network Structure Drive Protein Dynamics during Cytokinesis**

Vasudha Srivastava and Douglas N. Robinson



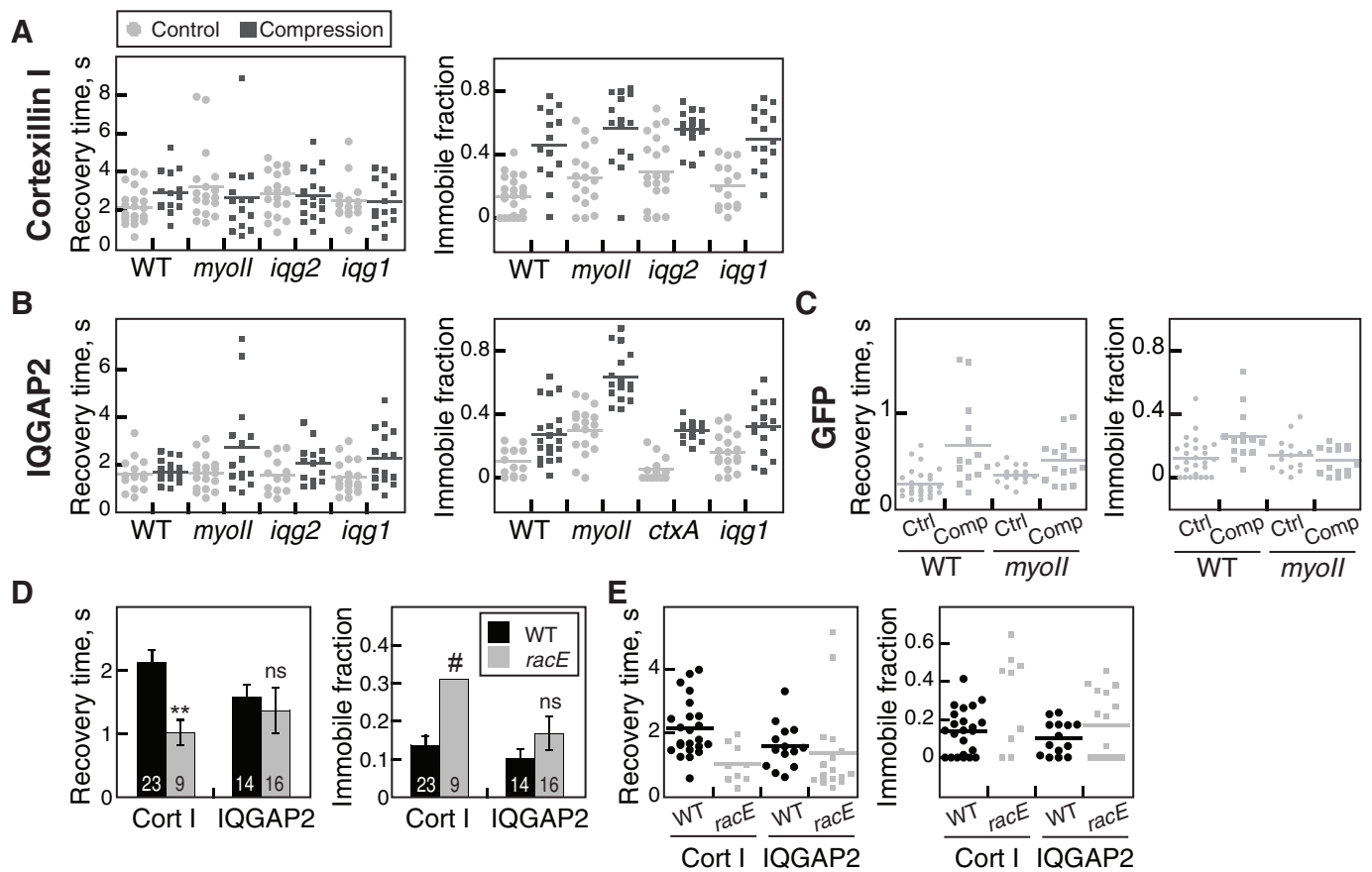
**Supplementary Figure S1, Related to Figure 1: FRAP and FCS calibration.** **(A)** An example confocal image of a GFP-cortixillin I-expressing cell illustrating the bleach, reference and background region used for FRAP measurements. **(B)** Example fluorescence intensity curves showing changes in intensity of bleached and reference regions during a FRAP experiment. **(C)** Example traces showing fluorescence recovery of GFP-cortixillin I in interphase and cleavage furrow cortex. **(D)** Distribution of recovery times and immobile fractions for various proteins in the cell cortex and the cytoplasm. **(E)** Distribution of recovery times and immobile fractions for GFP-actin and GFP in interphase, dividing, and compressed cells. **(F)** Example autocorrelation curves for rhodamine 6G diffusion as measured by FCS. The autocorrelation data was fitted to a 1-component 3D diffusion model with triplet state dynamics. The panel on right is the residual curve showing the goodness of fit. **(G)** The distribution of diffusion times and structural parameter measured for rhodamine 6G by FCS. **(H)** Diffusion times for purified mCherry and GFP-cortixillin I *in vitro*, and GFP and GFP-cortixillin I in cellular cytoplasm as measured by FCS. Calculated diffusion coefficients are provided in **Table S3**.



### Supplementary Figure S2, Related to Figure 2: Changes in cortexillin I and IQGAP2

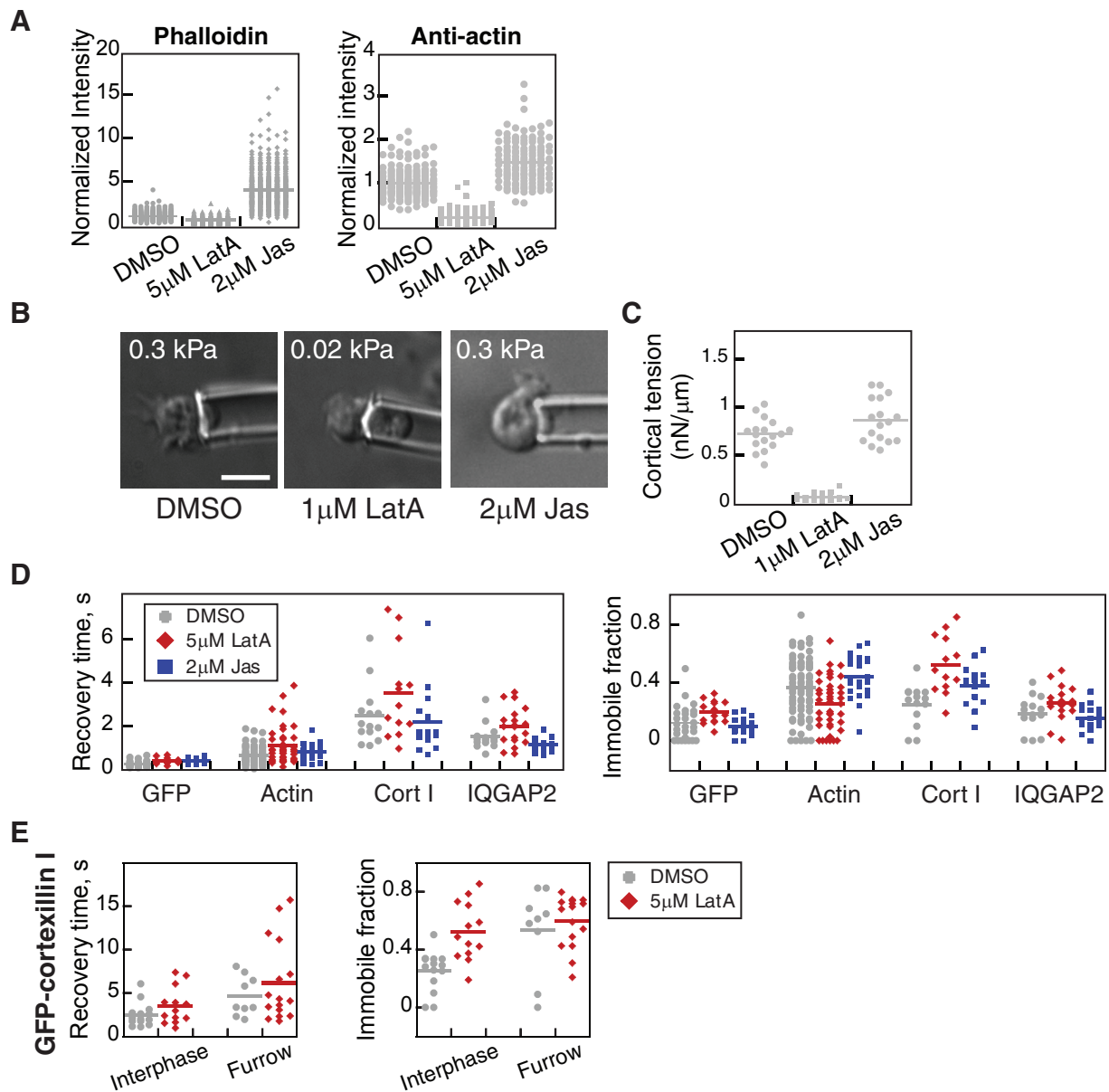
**dynamics at the cleavage furrow.** (A, B) Distribution of recovery times and immobile fractions for GFP-cortexillin I (A) and GFP-IQGAP2 (B) in different genetic mutants in interphase and dividing cell cortex. (C, D) Distribution of recovery times and immobile fractions for GFP-cortexillin I (C) and GFP-IQGAP2 (D) in WT, *myoII* and S456L *myoII* cells. (E) Distribution of recovery times and immobile fractions of GFP-actin in the interphase cortex of different mutants. (F) Mean recovery times and immobile fractions for GFP-cortexillin I in WT, *iqg2* single, and *iqg1/2* double mutants. (G) Distribution of recovery times and immobile fractions for GFP-cortexillin I in WT, *iqg2* single, and *iqg1/2* double mutants. Values plotted are mean  $\pm$  SEM; sample sizes are listed on the bars. *p* values are represented as ns: *p* > 0.05, \*: *p* < 0.05, \*\*: *p* < 0.005, \*\*\*: *p* < 0.0005 based on ANOVA with Fischer's LSD post-test.





### Supplementary Figure S3, Related to Figure 3: Changes in cortexillin I and IQGAP2

**dynamics under compression.** (A, B) Distribution of recovery times and immobile fractions for GFP-cortexillin I (A) and GFP-IQGAP2 (B) in different genetic mutants in control and compressed cells. (C) Distribution of recovery times and immobile fractions for GFP in WT and *myoII* cells without or with compression. (D) Average recovery times and immobile fractions of GFP-cortexillin I and GFP-IQGAP2 in WT and *racE* null cells. (E) Distribution of recovery times and immobile fractions of GFP-cortexillin I and GFP-IQGAP2 in WT and *racE* null cells. Values plotted are mean  $\pm$  SEM; sample sizes are listed on the bars. *p* values are represented as ns: *p* > 0.05, \*: *p* < 0.05, \*\*: *p* < 0.005, \*\*\*: *p* < 0.0005 based on ANOVA with Fischer's LSD post-test. #: The immobile fraction for cortexillin I in *racE* null cells is bimodal (see panel E); hence SEM is not shown.



**Supplementary Figure S4, Related to Figure 4: Changes in the actin network structure result in altered protein dynamics.** **(A)** Distribution of normalized fluorescence intensity for phalloidin and anti-actin staining in cells treated with DMSO, 5  $\mu$ M latrunculin-A and 2  $\mu$ M jasplakinolide **(B)** DIC images of micropipette aspiration experiments with DMSO, 1  $\mu$ M latrunculin-A and 2  $\mu$ M jasplakinolide **(C)** Cortical tension measurements for DMSO, 1  $\mu$ M latrunculin-A and 2  $\mu$ M jasplakinolide-treated cells **(D)** Distribution of recovery times and immobile fractions for GFP, GFP-actin, GFP-cortexillin I and GFP-IQGAP2 in DMSO, 5  $\mu$ M latrunculin-A or 2  $\mu$ M jasplakinolide-treated cells. **(E)** Distribution of recovery times and immobile fractions of GFP-cortexillin I in interphase and dividing cells with or without 5  $\mu$ M latrunculin-A.

**Table S1: Mean recovery times ( $\tau$ ) and mean immobile fractions ( $F_i$ ) for proteins in interphase cells, at the cleavage furrow and in compressed cells; FRAP Analysis**

**GFP-cortexillin I**

	Interphase	Furrow	Compression
WT	2.1 $\pm$ 0.2 s, 0.14 $\pm$ 0.02 (23)	4.7 $\pm$ 0.6 s, 0.36 $\pm$ 0.04 (17)	2.9 $\pm$ 0.3 s, 0.46 $\pm$ 0.06 (14)
<i>myoII</i>	3.2 $\pm$ 0.5 s, 0.26 $\pm$ 0.04 (18)	4.1 $\pm$ 0.3 s, 0.43 $\pm$ 0.04 (23)	2.6 $\pm$ 0.5 s, 0.57 $\pm$ 0.06 (15)
<i>iqg2</i>	2.9 $\pm$ 0.2 s, 0.29 $\pm$ 0.05 (21)	3.6 $\pm$ 0.3 s, 0.36 $\pm$ 0.05 (23)	2.7 $\pm$ 0.3 s, 0.56 $\pm$ 0.03 (17)
<i>iqg1</i>	2.5 $\pm$ 0.3 s, 0.20 $\pm$ 0.04 (15)	5.8 $\pm$ 0.9 s, 0.44 $\pm$ 0.05 (15)	2.4 $\pm$ 0.3 s, 0.50 $\pm$ 0.05 (15)
<i>iqg1/2</i>	2.4 $\pm$ 0.2 s, 0.27 $\pm$ 0.04 (23)	2.7 $\pm$ 0.4 s, 0.56 $\pm$ 0.05 (17)	
<i>racE</i>	1.1 $\pm$ 0.2 s, 0.31 $\pm$ 0.07 (9)		
S456L	3.4 $\pm$ 0.4 s, 0.34 $\pm$ 0.03 (23)		

**GFP-IQGAP2**

	Interphase	Furrow	Compression
WT	1.6 $\pm$ 0.2 s, 0.10 $\pm$ 0.02 (14)	2.1 $\pm$ 0.2 s, 0.48 $\pm$ 0.04 (16)	1.7 $\pm$ 0.1 s, 0.27 $\pm$ 0.04 (20)
<i>myoII</i>	1.6 $\pm$ 0.2 s, 0.30 $\pm$ 0.04 (18)	3.3 $\pm$ 0.3 s, 0.48 $\pm$ 0.05 (15)	2.7 $\pm$ 0.5 s, 0.64 $\pm$ 0.04 (15)
<i>ctxA</i>	1.5 $\pm$ 0.2 s, 0.06 $\pm$ 0.02 (13)	2.0 $\pm$ 0.3 s, 0.36 $\pm$ 0.04 (13)	2.1 $\pm$ 0.2 s, 0.30 $\pm$ 0.02 (14)
<i>iqg1</i>	1.5 $\pm$ 0.3 s, 0.16 $\pm$ 0.03 (18)	2.7 $\pm$ 0.3 s, 0.43 $\pm$ 0.04 (17)	2.3 $\pm$ 0.3 s, 0.33 $\pm$ 0.04 (16)
<i>racE</i>	1.4 $\pm$ 0.4 s, 0.17 $\pm$ 0.04 (16)		
S456L	1.8 $\pm$ 0.2 s, 0.22 $\pm$ 0.04 (13)		

**GFP-actin**

	Interphase	Furrow	Compression
WT	0.75 $\pm$ 0.15 s, 0.39 $\pm$ 0.05 (17)	1.3 $\pm$ 0.2 s, 0.28 $\pm$ 0.04 (17)	0.70 $\pm$ 0.06 s, 0.29 $\pm$ 0.01 (14)
<i>myoII</i>	0.68 $\pm$ 0.12 s, 0.43 $\pm$ 0.05 (11)		
<i>ctxA</i>	0.61 $\pm$ 0.12 s, 0.35 $\pm$ 0.05 (10)		
<i>iqg2</i>	0.46 $\pm$ 0.03 s, 0.34 $\pm$ 0.05 (15)		
<i>racE</i>	0.61 $\pm$ 0.18 s, 0.25 $\pm$ 0.07 (10)		

**GFP**

	Interphase	Furrow	Compression
WT	0.26 $\pm$ 0.03 s, 0.12 $\pm$ 0.02 (27)	0.27 $\pm$ 0.07 s, 0.12 $\pm$ 0.03 (12)	0.66 $\pm$ 0.12 s, 0.26 $\pm$ 0.04 (14)
<i>myoII</i>	0.35 $\pm$ 0.03 s, 0.14 $\pm$ 0.03 (15)		0.50 $\pm$ 0.06 s, 0.11 $\pm$ 0.02 (15)

The values represent mean  $\pm$  SEM for recovery times and immobile fractions. The number of measurements is given in parentheses.

**Table S2: Mean recovery times ( $\tau$ ) and mean immobile fractions ( $F_i$ ) for proteins latrunculin-A or jasplakinolide treated cells; FRAP Analysis**

	<b>DMSO</b>		<b>5 <math>\mu</math>M Latrunculin-A</b>		<b>2 <math>\mu</math>M Jasplakinolide</b>	
GFP cortl (interphase)	2.5 $\pm$ 0.4 s,	0.25 $\pm$ 0.04 (14)	3.5 $\pm$ 0.6 s,	0.53 $\pm$ 0.05 (13)	2.2 $\pm$ 0.4 s,	0.46 $\pm$ 0.06 (15)
GFP cortl (furrow)	4.6 $\pm$ 0.8 s,	0.53 $\pm$ 0.10 (9)	6.2 $\pm$ 1.1 s,	0.60 $\pm$ 0.04 (16)		
GFP IQGAP2	1.5 $\pm$ 0.2 s,	0.19 $\pm$ 0.03 (14)	2.0 $\pm$ 0.2 s,	0.26 $\pm$ 0.03 (19)	1.1 $\pm$ 0.1 s,	0.14 $\pm$ 0.02 (23)
GFP actin	0.66 $\pm$ 0.05 s,	0.36 $\pm$ 0.02 (68)	1.1 $\pm$ 0.13 s,	0.25 $\pm$ 0.03 (41)	0.82 $\pm$ 0.08 s,	0.44 $\pm$ 0.03 (22)
GFP	0.26 $\pm$ 0.03 s,	0.12 $\pm$ 0.02 (27)	0.40 $\pm$ 0.03 s,	0.20 $\pm$ 0.02 (15)	0.39 $\pm$ 0.03 s,	0.10 $\pm$ 0.02 (15)

The values represent mean  $\pm$  SEM for recovery times and immobile fractions. The number of measurements is given in parentheses.



**Table S3: Cytosolic diffusion times ( $\tau_D$ ) and diffusion coefficients ( $D_{eff}$ ) for proteins as measured by FCS**

**Diffusion in PBS at 22°C**

	<b>Molecular weight (kDa)</b>	<b>Diffusion time (<math>\tau_D</math>)</b>	<b>Diffusion Coefficient (<math>D_{eff}</math>)</b>
Rhodamine 6G	0.48 kDa	0.033 ± 0.002 ms (34)	426 $\mu\text{m}^2/\text{s}^*$
His-mCherry	28 kDa	0.15 ± 0.01 ms (11)	94 $\mu\text{m}^2/\text{s}$ (Reported value: 95 $\mu\text{m}^2/\text{s}^*$ )
His-GFP-cortexillin-I	80 kDa	0.28 ± 0.02 ms (11)	50.2 $\mu\text{m}^2/\text{s}$

**Diffusion in cytoplasm at 22°C**

<b>Cell line</b>	<b>Cortexillin I</b>	<b>IQGAP2</b>	<b>GFP</b>
WT control	2.4 ± 0.2 ms (20), $D_{eff} = 5.8 \mu\text{m}^2/\text{s}$	2.9 ± 0.3 ms (18), $D_{eff} = 4.8 \mu\text{m}^2/\text{s}$	0.78 ± 0.05 ms (20), $D_{eff} = 18 \mu\text{m}^2/\text{s}$
WT + compression	4.0 ± 0.3 ms (17), $D_{eff} = 3.5 \mu\text{m}^2/\text{s}$	3.4 ± 0.4 ms (16), $D_{eff} = 4.1 \mu\text{m}^2/\text{s}$	1.5 ± 0.1 ms (16), $D_{eff} = 9.4 \mu\text{m}^2/\text{s}$
<i>myoII</i>	2.6 ± 0.2 ms (18), $D_{eff} = 5.4 \mu\text{m}^2/\text{s}$	2.9 ± 0.2 ms (11), $D_{eff} = 4.8 \mu\text{m}^2/\text{s}$	1.4 ± 0.2 ms (15), $D_{eff} = 10 \mu\text{m}^2/\text{s}$
<i>myoII</i> + compression	3.9 ± 0.4 ms (12), $D_{eff} = 3.6 \mu\text{m}^2/\text{s}$	-	0.69 ± 0.06 ms (14), $D_{eff} = 20 \mu\text{m}^2/\text{s}$
<i>iqg2</i>	3.1 ± 0.2 ms (16), $D_{eff} = 4.5 \mu\text{m}^2/\text{s}$	-	-
<i>iqg1/2</i>	3.7 ± 0.3 ms (16), $D_{eff} = 3.8 \mu\text{m}^2/\text{s}$	-	-
<i>ctxA</i>	-	2.6 ± 0.3 ms (12), $D_{eff} = 5.4 \mu\text{m}^2/\text{s}$	-

<b>Treatment</b>	<b>Cortexillin I</b>	<b>IQGAP2</b>	<b>GFP</b>
DMSO	2.8 ± 0.4 ms (12), $D_{eff} = 5.0 \mu\text{m}^2/\text{s}$	2.7 ± 0.4 ms (15), $D_{eff} = 5.2 \mu\text{m}^2/\text{s}$	0.75 ± 0.10 ms (13), $D_{eff} = 19 \mu\text{m}^2/\text{s}$
5 $\mu\text{M}$ latrunculin-A	P1: 2.4 ± 0.1 ms (8), $D_{eff} = 5.8 \mu\text{m}^2/\text{s}$ P2: 8.1 ± 0.5 ms (7), $D_{eff} = 1.7 \mu\text{m}^2/\text{s}$	3.6 ± 0.4 ms (16), $D_{eff} = 3.9 \mu\text{m}^2/\text{s}$	1.1 ± 0.1 ms (25), $D_{eff} = 13 \mu\text{m}^2/\text{s}$
2 $\mu\text{M}$ jasplakinolide	3.2 ± 0.2 ms (20), $D_{eff} = 4.4 \mu\text{m}^2/\text{s}$	3.2 ± 0.4 ms (18), $D_{eff} = 4.4 \mu\text{m}^2/\text{s}$	0.86 ± 0.07 ms (18), $D_{eff} = 16 \mu\text{m}^2/\text{s}$

The values represent mean ± SEM for diffusion times. The numbers of measurements is given in parentheses.

\* Diffusion coefficients for rhodamine 6G and GFP were reported in Petrášek and Schwillé (2008) [S1].

**Table S4: Cell strains used in this study**

Strain	Genotype	Experimental Applications
WT	Ax3(Rep orf+)	Phalloidin staining/F-actin quantification; MPA (cortical tension)
WT::GFP	Ax3(Rep orf+)::Hyg <sup>R</sup> :pDRH; GFP, G418 <sup>R</sup> :pDM181	FRAP, FCS
WT::GFP	<i>myoII</i> (HS1)::mCH- <i>myoII</i> , Hyg <sup>R</sup> :pDRH; GFP, G418 <sup>R</sup> :pDM181	FRAP
WT::GFP-actin	KAx3(RF)::Hyg <sup>R</sup> :pDRH; GFP-actin, G418 <sup>R</sup> :pDM181	FRAP
WT::GFP-actin	<i>myoII</i> (HS1)::mCH- <i>myoII</i> , Hyg <sup>R</sup> :pDRH; GFP-actin, G418 <sup>R</sup> :pDM181	FRAP
WT::GFP-cortexillin I	KAX3(RF)::GFP-cortI, Hyg <sup>R</sup> :pDRH; G418 <sup>R</sup> :pDM181	FRAP, FCS
WT::GFP-IQGAP2	KAX3::RFP- $\alpha$ -tubulin, Hyg <sup>R</sup> :pDRH; GFP-IQGAP2, G418 <sup>R</sup> :pEXP4	FRAP, FCS
<i>myoII</i> ::GFP-actin	<i>myoII</i> (HS1)::RFP- $\alpha$ -tubulin, Hyg <sup>R</sup> :pDRH; GFP-actin, G418 <sup>R</sup> :pDM181	FRAP
<i>myoII</i> ::GFP-cortexillin I	<i>myoII</i> (HS1)::GFP-cortI, Hyg <sup>R</sup> :pDRH; G418 <sup>R</sup> :pDM181	FRAP, FCS
<i>myoII</i> ::GFP-IQGAP2	<i>myoII</i> (HS1)::RFP- $\alpha$ -tubulin, Hyg <sup>R</sup> :pDRH; GFP-IQGAP2, G418 <sup>R</sup> :pEXP4	FRAP, FCS
<i>myoII</i> ::GFP	<i>myoII</i> (HS1)::Hyg <sup>R</sup> :pDRH; GFP, G418 <sup>R</sup> :pDM181	FRAP, FCS
S456L::GFP-cortexillin I	<i>myoII</i> (HS1)::GFP-cortI, Hyg <sup>R</sup> :pDRH; <i>myoII</i> (S456L), G418 <sup>R</sup> :pBIG	FRAP
S456L::GFP-IQGAP2	<i>myoII</i> (HS1)::CFP- <i>myoII</i> (S456L), Hyg <sup>R</sup> :pDRH; GFP-IQGAP2, G418 <sup>R</sup> :pEXP4	FRAP
<i>ctxA</i> ::GFP-actin	<i>cortI</i> (RF)::RFP- $\alpha$ -tubulin, Hyg <sup>R</sup> :pDRH; GFP-actin, G418 <sup>R</sup> :pDM181	FRAP
<i>ctxA</i> ::GFP-IQGAP2	<i>cortI</i> (RF)::RFP- $\alpha$ -tubulin, Hyg <sup>R</sup> :pDRH; GFP-IQGAP2, G418 <sup>R</sup> :pEXP4	FRAP, FCS
<i>iqg2</i> ::GFP-actin	<i>iqgap2</i> (RF)::RFP- $\alpha$ -tubulin, Hyg <sup>R</sup> :pDRH; GFP-actin, G418 <sup>R</sup> :pDM181	FRAP
<i>iqg2</i> ::GFP-cortexillin I	<i>iqgap2</i> (RF)::GFP-cortI, Hyg <sup>R</sup> :pDRH; G418 <sup>R</sup> :pDM181	FRAP, FCS
<i>iqg1</i> ::GFP-cortexillin I	<i>iqgap1</i> (RF)::GFP-cortI, Hyg <sup>R</sup> :pDRH; G418 <sup>R</sup> :pDM181	FRAP
<i>iqg1</i> ::GFP-IQGAP2	<i>iqgap1</i> (RF)::RFP- $\alpha$ -tubulin, Hyg <sup>R</sup> :pDRH; GFP-IQGAP2, G418 <sup>R</sup> :pEXP4	FRAP
<i>iqg1/2</i> ::GFP-cortexillin I	<i>iqgap1/2</i> (RF)::GFP-cortI, Hyg <sup>R</sup> :pDRH; G418 <sup>R</sup> :pDM181	FRAP, FCS
<i>racE</i> ::GFP-actin	<i>racE</i> <sup>24EH6</sup> ::RFP- $\alpha$ -tubulin, Hyg <sup>R</sup> :pDRH; GFP-actin, G418 <sup>R</sup> :pDM181	FRAP
<i>racE</i> ::GFP-cortexillin I	<i>racE</i> <sup>24EH6</sup> ::GFP-cortI, Hyg <sup>R</sup> :pDRH; G418 <sup>R</sup> :pDM181	FRAP
<i>racE</i> ::GFP-IQGAP2	<i>racE</i> <sup>24EH6</sup> ::RFP- $\alpha$ -tubulin, Hyg <sup>R</sup> :pDRH; GFP-IQGAP2, G418 <sup>R</sup> :pEXP4	FRAP

## Supplemental Experimental Procedures

### Cell strains and Culture

A complete list of the strains used is provided in **Supplementary Table S4**. Cells were grown in Hans' enriched 1.5X HL-5 media (enriched with 8% FM) containing penicillin and streptomycin at 22°C on polystyrene petri dishes. Wild type strains used were KAx3 [S2], Ax3:Rep orf+ (HS1000) [S3] and rescued strains. Mutant cell lines used have been described previously – *myoII* [2], *ctxA*, *ctxB*, and *ctxA/B* [S3, S4], *iqg1*, *iqg2* and *iqg1/2* [S4], and *racE* [S3]. The plasmids for RFP-tubulin, GFP-cortexillin-I, GFP-IQGAP2, GFP-actin, mCherry-myosin-II and GFP have been described previously [S4-S7]. Cells were transformed with expression plasmids by electroporation using a Genepulser-II electroporator (Bio-Rad, Hercules, CA). Cells were then grown in selection medium containing 15 µg/mL G418 or 40 µg/mL hygromycin or both drugs when transforming two plasmids. Expression levels were checked by fluorescence imaging or Western blotting. Cells with comparable fluorescent protein expression were used for the experiments.

### Compression by Agarose Overlay

Agarose overlay has been established as a method for applying uniform global mechanical stress, and has previously been shown to drive mechanosensitive accumulation of certain proteins at the cell cortex [S6]. For compression, thin sheets of 2% agarose in MES starvation buffer (50 mM MES pH 6.8, 2 mM MgCl<sub>2</sub> and 0.2 mM CaCl<sub>2</sub>) were prepared according to the protocol described by Fukui *et al.* [8, 9] and modified by Kee *et al.* [S6]. The cells were plated in imaging chambers for 1 hour. The culture medium was aspirated and cells were washed with MES starvation buffer twice to reduce the background fluorescence. The buffer was removed completely and a sheet of agarose was carefully placed to cover the cells. Imaging was started after the cells were completely flattened (about 2 minutes). The slide was replaced every 10 minutes to ensure proper cell health.

### Latrunculin-A and Jasplakinolide Treatment

Latrunculin-A and Jasplakinolide were obtained from Sigma-Aldrich. All cells were pre-treated with 0.1% DMSO for 4-6 hours. For phalloidin and anti-actin staining, the cells were incubated with the drugs for 15 minutes. For live cell imaging, drug stocks were freshly made in MES starvation buffer. The cells plated in imaging chambers were washed with MES starvation buffer + 0.1% DMSO, followed by the addition of the drug-containing buffer. Imaging was performed after 10 minute incubation, and each slide was imaged for 15 minutes before it was replaced with a new slide.

### Fluorescence Recovery after Photobleaching (FRAP)

FRAP experiments were performed using a Zeiss Axiovert 200 inverted microscope with LSM510-Meta confocal module, with a 63x (NA 1.4) objective. Cells expressing GFP-tagged proteins were plated in glass-bottom imaging chambers for an hour. The culture medium was replaced with MES starvation buffer immediately before imaging. A small region of the cell cortex was bleached using a 488 nm Argon laser, and the fluorescence recovery was recorded until recovery saturated (150 frames, 45-150 ms/frame depending on the protein). The size and placement of the bleach region was kept relatively constant across measurements.

For each frame, the average intensity of the bleached cortical region, reference (unbleached) region, and background was quantified using ImageJ (National Institutes of Health, Bethesda, MD) (**Fig. S1A-B**). For photobleaching correction, the reference theoretical intensity (RTI) was calculated by fitting the background subtracted reference intensity to an exponential decay equation as follows:

$$RTI(t) = A - B \cdot e^{-C \cdot t} \quad (1)$$

Where, A, B and C are fitting parameters.

The intensity of the bleached region was background subtracted and normalized to RTI (**Fig. S1C**). The normalized intensity (NI) was obtained by normalizing this to the pre-bleach intensity (average of 4 pre-bleach images), and was fitted to a single exponential as follows:

$$NI(t) = m_1(1 - m_2 \cdot e^{-kt}) \quad (2)$$

Where,  $m_1$ ,  $m_2$  are fitting parameters and k is the recovery rate.

The recovery time,  $\tau$ , and the immobile fraction,  $F_i$  were measured as:

$$\text{Recovery time, } \tau = 1/k \quad (3)$$

$$\text{Immobile fraction, } F_i = \frac{1-m_1}{1-m_1+m_2} \quad (4)$$

We also plotted the derivative of normalized intensity for each protein to confirm that our data fit a single-exponential, and did not require more complicated models.

### Fluorescence Correlation Spectroscopy (FCS)

FCS experiments were performed using a Zeiss AxioObserver with 780-Quasar confocal module & FCS, with a C-Apochromat 40x (NA 1.2) water objective. For purified proteins and dyes, the imaging plane was set 200  $\mu\text{m}$  above the coverslip. 10 repetitions of 5 seconds each were collected and the



average spectrum was used for measuring diffusion times. For diffusion measurements in cells, the imaging plane was set through the middle of the cell. The acquisition time was reduced to 2 seconds to avoid complications from long distance cellular and intracellular movement. The average from 2-7 repetitions was used to calculate diffusion times. Any trace showing a persistent deviation from the mean or significant photobleaching was discarded. The autocorrelation data was then fit to a single component, 3D-diffusion model with triplet state dynamics using the following equation:

$$g(\tau) = G_{triplet} \cdot \frac{1}{N} \cdot \left(1 + \frac{\tau}{\tau_D}\right)^{-1} \cdot \left(1 + \frac{\tau}{\gamma^2 \tau_D}\right)^{-0.5} \quad (5)$$

Where,

$\tau$  = correlation time

$\tau_D$  = diffusion time

$N$  = number of particles

$\gamma$  = structural parameter

$$G_{triplet} = \frac{1 - \theta_T + \theta_T \cdot e^{-\tau/\tau_T}}{\theta_T}$$

( $\theta_T$  = fraction of particles in triplet state and  $\tau_T$  = relaxation time for triplet state).

100 nM Rhodamine 6G was used for pinhole alignment and structural parameter calculation (**Fig. S1F-H**). The measured value of the structural parameter was used for diffusion time calculation of other proteins. All imaging was done in uncoated 35 mm-glass bottom dishes (Coverslip No. 1.5) (MatTek Corp., Ashland, MA).

In compressed cells, the cell height is comparable to the z-dimension of the FCS confocal volume. Therefore, we also analyzed the FCS data using a 2D-diffusion model and observed no significant differences in diffusion times as compared to those calculated using the 3D-diffusion model.

### Calculation of Diffusion Coefficients

Rhodamine 6G was used as a standard for calculating diffusion coefficients. As the diffusion coefficient is inversely proportional to the diffusion time, we used the published value of the diffusion coefficient for rhodamine 6G and measured diffusion times for rhodamine 6G and the proteins of interest to calculate effective diffusion coefficients ( $D_{eff}$ ).

$$D_{eff} = \frac{D_{R6} \cdot \tau_{D,R6}}{\tau_D} \quad (6)$$

Where,

$D_{R6}$  = diffusion coefficient for rhodamine 6G (= 426  $\mu\text{m}^2/\text{s}$  [S1])

$\tau_{D,R6}$  = measured diffusion time for rhodamine 6G =  $33 \pm 2 \mu\text{s}$

$\tau_D$  = measured diffusion time.

We used purified mCherry to validate our diffusion coefficient calculation. Our measured diffusion coefficient for mCherry ( $94 \mu\text{m}^2/\text{s}$ ) matched closely the published value for purified GFP ( $95 \mu\text{m}^2/\text{s}$  [S1]) under the same conditions (**Supplemental Table S3**).

### **Phalloidin and Anti-actin Staining for F-actin Quantification**

For quantifying the relative amount of F-actin, the cells were fixed and stained with TRITC-phalloidin (Sigma Aldrich) or anti-actin monoclonal antibody (Developmental Studies Hybridoma Bank, University of Iowa) as described in *Luo et al.* [10]. *Dictyostelium* cells were plated on sterile 22x22 mm glass coverslips in 6-well polystyrene dishes at 70-80% confluency for 1 hour. The media was aspirated and replaced with 2 mL drug-containing media for 15 minutes. The cells were washed with 1X PBS, and immediately fixed on ice using acetone at  $-20^\circ\text{C}$  for 3 minutes. The coverslips were transferred to a new 6-well dish and washed once with 1X PBS, followed by blocking in blocking buffer (1X PBS + 0.05% Triton X-100 + 0.5% BSA) for 30 min. The cells were stained with  $0.16 \mu\text{M}$  TRITC-phalloidin for 1 hour or with anti-actin antibody overnight followed by 2 hour incubation with TRITC goat-anti-mouse secondary. All coverslips were washed 4 times with 1X PBT (1X PBS + 0.05% Triton X-100) for 5 minutes each, and then once with 1X PBS. The coverslips were then mounted on glass slides using 10  $\mu\text{L}$  mounting buffer (90% glycerol in 1X PBS).

To quantify the relative amount of F-actin, all coverslips were imaged under identical conditions on a motorized Olympus IX71 microscope using a 40x (NA 1.3) objective with a 1.6x optovar (Olympus, Center Valley, PA). The integrated fluorescence intensity of the cells was quantified using ImageJ. At least 100 cells from more than 10 different fields were quantified. The intensity was normalized to the average fluorescence intensity of the untreated control for a given experiment. The data shown represents three biological replicates.

### **Cortical Tension Measurement Using Micropipette Aspiration**

The experimental set-up has been previously described in detail in Effler *et al.* (2006) [S5].  $0.01\text{-}0.6 \text{ nN}/\mu\text{m}^2$  pressures were applied to a smooth region of the cell cortex through a  $\sim 5 \mu\text{m}$  internal diameter glass micropipette ( $R_p = 2.3\text{-}3 \mu\text{m}$ ). A low pressure was first applied to form a pressure seal. The cell protrusion was allowed to stabilize for 30 seconds before imaging. Subsequently, the pressure was gradually increased and imaging was resumed after the protrusion stabilized. This

was continued until the protrusion length became large ( $L_p > R_p$ ) or the cell blebbed. At each pressure, the protrusion length from five consecutive frames was averaged. The critical pressure ( $\Delta P_{crit}$ ) was identified as the pressure where  $L_p = R_p$ , and the cortical tension ( $T_{eff}$ ) was calculated using the following equation:

$$\Delta P_{crit} = 2T_{eff} \cdot \left( \frac{1}{R_p} - \frac{1}{R_c} \right) \quad (7)$$

### Supplemental References

- S1. Petrášek, Z., and Schwille, P. Precise Measurement of Diffusion Coefficients using Scanning Fluorescence Correlation Spectroscopy. *Biophysical Journal* 94, 1437-1448.
- S2. Ruppel, K.M., Uyeda, T.Q., and Spudich, J.A. (1994). Role of highly conserved lysine 130 of myosin motor domain. In vivo and in vitro characterization of site specifically mutated myosin. *Journal of Biological Chemistry* 269, 18773-18780.
- S3. Robinson, D.N., and Spudich, J.A. (2000). Dynacortin, a Genetic Link between Equatorial Contractility and Global Shape Control Discovered by Library Complementation of a *Dictyostelium discoideum* Cytokinesis Mutant. *J. Cell Biol.* 150, 823-838.
- S4. Lee, S., Shen, Z., Robinson, D.N., Briggs, S., and Firtel, R.A. (2010). Involvement of the Cytoskeleton in Controlling Leading-Edge Function during Chemotaxis. *Molecular Biology of the Cell* 21, 1810-1824.
- S5. Effler, J.C., Kee, Y.-S., Berk, J.M., Tran, M.N., Iglesias, P.A., and Robinson, D.N. (2006). Mitosis-Specific Mechanosensing and Contractile-Protein Redistribution Control Cell Shape. *Current Biology* 16, 1962-1967.
- S6. Kee, Y.-S., Ren, Y., Dorfman, D., Iijima, M., Firtel, R., Iglesias, P.A., and Robinson, D.N. (2012). A mechanosensory system governs myosin II accumulation in dividing cells. *Molecular Biology of the Cell* 23, 1510-1523.
- S7. Luo, T., Mohan, K., Iglesias, P.A., and Robinson, D.N. (2013). Molecular mechanisms of cellular mechanosensing. *Nat Mater* 12, 1064-1071.
- S8. Fukui, Y., Yumura, S., Yumura, T.K., and Mori, H. (1986). Agar overlay method: high-resolution immunofluorescence for the study of the contractile apparatus. *Methods Enzymol* 134, 573-580.
- S9. Fukui, Y., Yumura, S., and Yumura, T.K. (1987). Agar-overlay immunofluorescence: high-resolution studies of cytoskeletal components and their changes during chemotaxis. *Methods Cell Biol* 28, 347-356.
- S10. Luo, T., Mohan, K., Srivastava, V., Ren, Y., Iglesias, P.A., and Robinson, D.N. (2012). Understanding the Cooperative Interaction between Myosin II and Actin Cross-Linkers Mediated by Actin Filaments during Mechanosensation. *Biophysical Journal* 102, 238-247.